Ductile damage model calibration for high-strength structural steels

Yang, Fei; Veljkovic, Milan; Liu, Yuqing

Important note
To cite this publication, please use the final published version (if applicable).
Please check the document version above.

Ductile damage model calibration for high-strength structural steels

Fei Yang [a,b], Milan Veljkovic [b], Yuqing Liu [a,*]

[a] *Department of Bridge Engineering, Tongji University, Shanghai, China*
[b] *Department of Engineering Structures, Delft University of Technology, Delft, the Netherlands*

HIGHLIGHTS

- Post-necking true stress–strain relations of four structural steels are investigated.
- The combined linear and power law is used to describe the post-necking stress–strain relations of steels.
- A ductile damage model is proposed to simulate the damage and fracture of steels.
- The fracture of tensile coupons of the investigated steels is simulated.

ARTICLE INFO

ABSTRACT

Numerical analyses incorporating appropriate damage models provide an opportunity to predict the strength and deformation capacity of steel structures. This paper presents a practical calibration for the ductile damage model of S355 and high-strength steel S690Q, S700MC, S960Q based on tensile coupon test results. A combined linear and power expression is adopted to calibrate the post-necking damaged stress–strain relations of the investigated steels, upon which the undamaged stress–strain relations are estimated further. Damage initiation criterion is based on the Rice-Tracey model and damage evolution law is related to the calibrated damaged stress and the estimated undamaged stress. Fracture of the tensile coupons is modelled using a critical damage variable. Tensile coupon tests on the investigated steels are modelled in ABAQUS with the explicit solver. Results show that combining the proposed post-necking stress–strain relations and ductile damage model generates very good predictions for strain localization and final fracture of the tensile coupons. Numerical engineering stress–strain curves agree well with the experimental results. It also indicates that high-strength steels are more susceptible to damage than S355. The damage variable of S960Q is about 2 times as large as that of S355 from the onset of necking to the final fracture.

© 2020 Elsevier Ltd. All rights reserved.

1. Introduction

High-strength steels (HSS) have been widely used in engineering structures (offshore structures, building and bridge structures, etc.) and engineering equipment (engineering vehicles, crane facilities, etc.) [1–4]. Application of HSS has the potential to reduce plate thickness in welded structures for saving welding costs and to support much higher external loads for realizing more innovative structures. HSS are normally manufactured by quenching and tempering (Q&T) process or thermo-mechanically controlled process (TMCP) [5–7]. The progress of these two processes promotes the massive application of HSS. The microstructure of HSS is different from that of conventional mild steels due to special manufacturing process, resulting in an improved tensile strength at the expense of material ductility. Therefore, the plastic design method for structures using mild steels may not be fully applicable to the design of HSS structures. The effect of less material ductility of HSS on structural resisting performance is one of the major concerns for practical applications [8–11].

The variation of structural strength and deformation, resulted from the occurrence and evolution of material damage, could be numerically predicted by incorporating appropriate steel damage or fracture models [12–22]. Kanvinde et al. [12–14] investigated the applicability and accuracy of two micromechanics-based ductile fracture models, the stress modified critical strain (SMCS) model and void growth model (VGM), for predicting the crack initiation of structural steels at locations without macroscopic initial flaws. Both models integrate plastic strains and triaxial stresses to predict crack initiation, and the former only uses the critical values

* Corresponding author.
  E-mail address: yql@tongji.edu.cn (Y. Liu).

while the latter considers the loading histories of plastic strains and triaxial stresses. The uniaxial true stress–strain relation plays an essential role in the simulation of ductile fracture predictions due to large deformations occurring in strain localization regions. However, the calibration of true stress–strain relation for each structural steel was not implemented in detail before the parameter identification for the fracture models, which might lead to some deviations for the identified parameters in the fracture models [12–16].

The GTN damage model is a micromechanics-based porous plasticity model considering the effect of void growth and coalescence through the coupling of material yield surface and hydrostatic stress. It was initially proposed by Gurson [17] and then modified by Tvergaard and Needleman [18] through introducing a failure point after which the effect of hydrostatic stress on yield surface accelerates. Achouri et al. [19,20] reported an experimental study on the ductile damage mechanism of a high-strength low-alloy steel and a parameter identification strategy for the GTN model was calibrated based on the experimental results of notched specimens. The calibrated GTN model shows very good prediction capability over a wide range of stress states. Feldman and Schaffrath [21,22] recently applied the GTN model in the simulation of strength and deformation capacity of centre-holed HSS plates under tensile loading. The numerical load–displacement curves agree well with the experimental results even including the post-fracture stages. Although the GTN model could be used in the damage and fracture simulation of steel structures, there are at least 7 parameters that must be identified for each steel [19] and the commonly performed tensile coupon tests cannot offer enough results for the parameter identification, which makes it inconvenient to apply in the simulation of steel structures. Besides, the uniaxial true stress–strain relation in the GTN model should be input as the material constitutive in the absence of damage since the effect of void growth and coalescence is considered by the variable of void volume fraction in the model. The "undamaged material constitutive" in large deformations cannot be measured in experiments and the strain hardening property is generally assumed as a power law [19], which would increase the deviations of parameter identification in the GTN model.

Tensile coupon tests are commonly conducted to determine the stress–strain relation and basic mechanic properties of steels [23]. Hertelé et al. [24] made a complete review of the conventional stress–strain models including Ludwik, Ramberg-Osgood, Hollomon, Voce, Swift, and Ludwigson model, which are commonly used to describe the stress–strain relation in the initial strain-hardening stage. Afterward, a generic stress–strain model with two-stage strain-hardening was proposed allowing an accurate description of pre-necking stress–strain relations. Yun and Gardner [25,26] recently investigated the pre-necking engineering stress–strain relations of hot-rolled and cold-formed structural steels by analysing a large number of experimental stress–strain curves collected from the literature. A quad-linear constitutive expression and a bilinear plus nonlinear hardening expression were proposed and calibrated for hot-rolled steels, in which parameters were only dependent on Young's modulus, yield stress and ultimate stress. A two-stage Ramberg-Osgood constitutive model was calibrated to describe the engineering strain-strain relations of cold-formed steels. In practice, the pre-necking true stress–strain relation for numerical analysis can be converted from the measured pre-necking engineering stress–strain relation based on tensile coupon tests. Actually, the post-necking true stress–strain relation is also necessary for simulations when structural behaviours undergoing large deformations or the damage and fracture behaviours are analysed. However, the post-necking relation is commonly taken as an extrapolation of the pre-necking stress–strain relation [19,27,28] or a linear curve from the true stress–strain at the onset

of necking to the fracture stress–strain derived upon the assumption that fracture true stress and strain are uniform at the critical necking section [15–16]. Therefore, the post-necking behaviours are worth being investigated further for the damage and fracture analysis of steel structures.

From the perspective of continuum damage mechanics [29–31], the process from the onset of necking to the fracture of a tensile coupon can be considered as a ductile damage process with void nucleation, growth and coalescence in the necking region. Accordingly, the post-necking stress–strain relations and ductile damage behaviours of steels are worth being explored and calibrated based on the tensile coupon test results in the load-descending phase, since they are essential to numerically assess the structural resistance and deformation capacity. The objective of this paper is to present a practical calibration of the phenomenological damage model for HSS using the full-range engineering stress–strain curves from tensile coupon tests. S355 and HSS grade S690Q, S700MC, S960Q are analysed based on the available experimental results reported in [32–34]. A combined linear and power stress–strain law is adopted to describe the post-necking damaged and undamaged stress–strain relations with respective calibrated weighting factors. Fracture of tensile coupons is modelled using a critical damage variable. The proposed damage models are validated against the experimental results of tensile coupon tests and the damage properties of each steel are discussed.

2. Post-necking stress–strain relations

2.1. Experimental results

Tensile coupon test results of some HSS reported recently are used here to investigate the post-necking behaviours mainly including the material plasticity and damage performance. Ho et al. [33] performed tensile coupon tests on S690Q and the full-range engineering stress–strain curves was reported. In the RUOSTE project [34], material ductility requirements for S700MC and S960Q were investigated. S700MC is a thermo-mechanically rolled structural steel made for cold-forming [35] and S960Q is a structural steel produced by quenching and tempering process [6]. Besides, Ribeiro et al. [32] investigated the mechanical properties of the massively used non-alloy structural steel S355 [36]. In the above studies, full-range engineering stress–strain curves of the investigated steels were reported. S690Q, S700MC, and S960Q HSS are the main research objects of this paper. S355 is also included to compare the mechanical properties between HSS and mild steel.

Fig. 1 shows the major geometries and dimensions of the tensile coupons in [32–34]. For S355 coupon, the parallel part has a cross-section of 15 × 20 mm. The initial gauge length and parallel length are 50 and 90 mm, respectively. For S690Q coupon, the parallel part has a 10 × 6 mm cross-section. The gauge length is 43.75 mm, a little less than the parallel length of 50 mm. Same geometry is adopted for S700MC and S960Q coupons with a cross-section of 30 × 8 mm at the parallel parts. The initial gauge length and parallel length are 80 and 100 mm, respectively. Digital imaging correlation technique or extensometers were used to measure the elongations of gauge length during the entire loadings. It needs to be clarified that tensile coupons shown in Fig. 1 are the geometric models in the finite element analysis (FEA) instead of the actual coupon geometries. The difference is that the axial dimension of coupon grip parts is only about 1/3 of the actual dimension since the main concern of the FEA is the parallel parts of tensile coupons.

Fig. 2 depicts the experimental full-range engineering stress–strain curves for S355, S690Q, S700MC, and S960Q adapted from
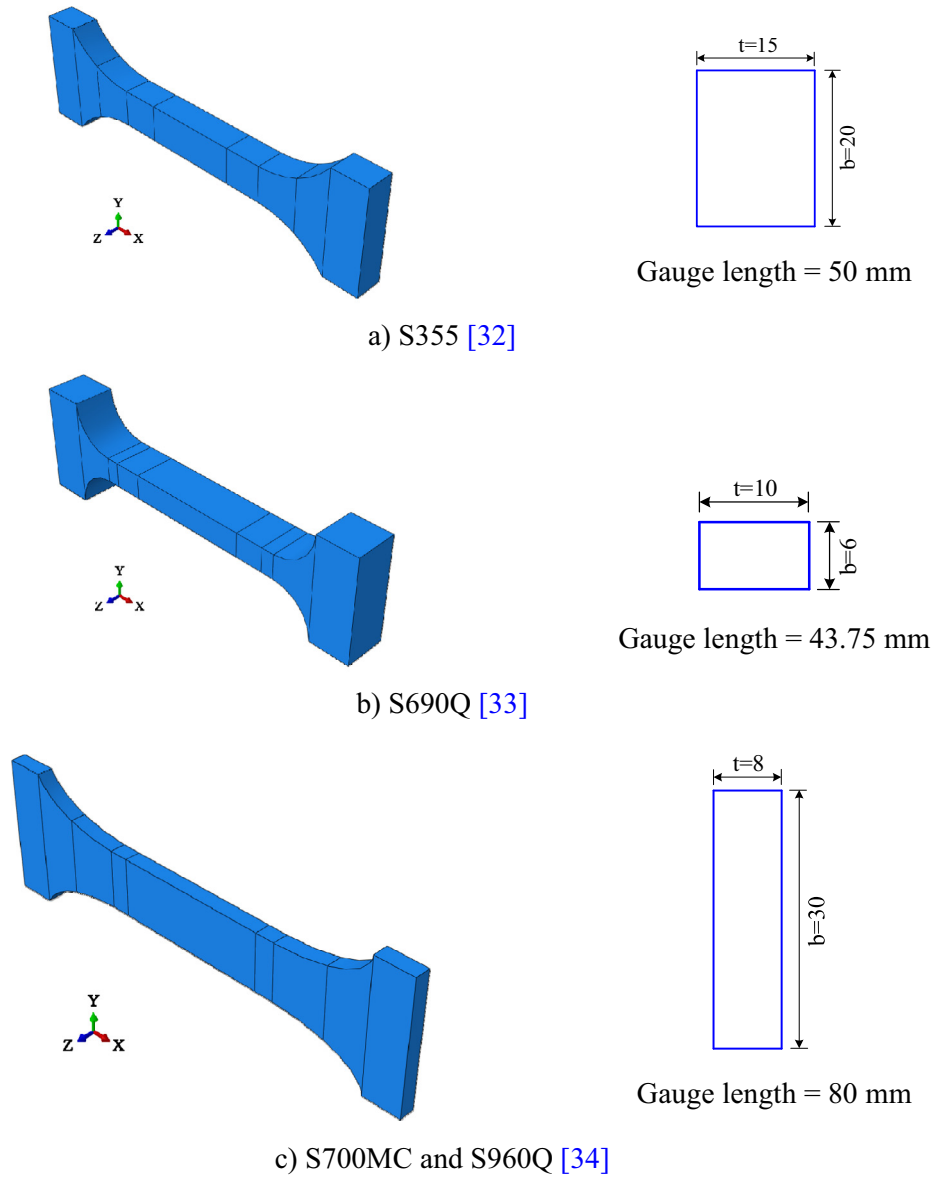
a) S355 [32]

Gauge length = 50 mm

b) S690Q [33]

Gauge length = 43.75 mm

c) S700MC and S960Q [34]

Gauge length = 80 mm

Fig. 1. Geometries and dimensions of tension coupons (Unit: mm).
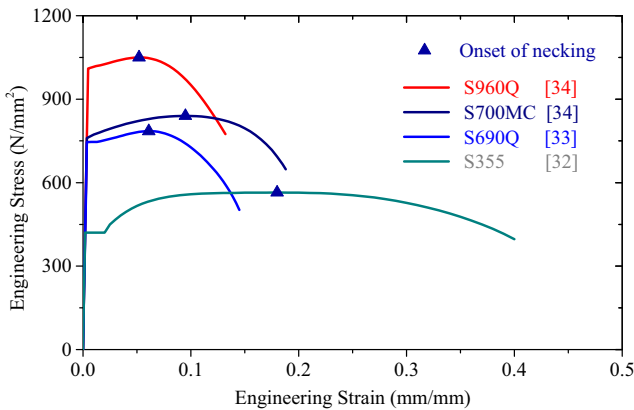

Fig. 2. Engineering stress–strain curves (). adapted from [32–34]

[32–34]. In the tests the elongations of gauge lengths were measured through displacement monitoring systems until the fracture of tensile coupons. Table 1 lists the experimental material proper-

ties of each steel. Three coupon tests for S355 were reported in [32] and the experimental stress–strain curve of 2# specimen was selected for the following analysis. Two coupon tests for S690Q were reported in [33] and the experimental stress–strain curves were almost identical except for an evident difference for the strain at ultimate strength. Given that the following calibration of post-necking stress–strain relations is related to the strain at ultimate strength, an average strain at ultimate strength equal to 6.1%, as listed in Table 1, is considered for analysis. Hence, the engineering stress–strain curve for S690Q shown in Fig. 2 is an average curve of the experimental results in [33].

The engineering strain at fracture of each HSS is much less than that of S355, see Fig. 2. No obvious yield plateau exists in the engineering stress–strain curves of S960Q and S700MC. Besides, the post-necking engineering stress for HSS has a larger decreasing rate compared to S355. The material properties listed in Table 1 indicate that the ultimate-to-yield ratios of S690Q and S960Q are about 1.05, much less than 1.35 for S355. The strains at ultimate strength and fracture for S700MC are both larger than the corresponding strains for S690Q. The ultimate-to-yield ratio for

Table 1
Experimental material properties (according to [32–34]).

Material properties	S355	S690Q	S700MC	S960Q
Young's modulus E (N/mm^2)	210 000	205 000	214 000	214 000
Yield strength f_y (N/mm^2)	420	746	760	1010
Ultimate strength f_u (N/mm^2)	565	785	840	1050
Strain at ultimate strength ε_u (%)	18.0	6.1	9.5	5.2
Strain at fracture ε_f (%)	40.0	14.5	18.8	13.2

S700MC is about 1.10, which is larger than 1.05 for S690Q. Despite almost similar yield strength of S700MC and S690Q, the ductility of S700MC is better owing to its higher fracture strain compared to S690Q.

It needs to be clarified that the geometry and gauge length of tensile coupons affect the post-necking engineering stress–strain curves. In addition, the loading rate in tensile coupon tests also has effects on the uniaxial plastic behaviours [23,37]. Recently experimental results indicate that the stress–strain relation of S690 shows a loading rate dependency and the yield and tensile strength would grow significantly as the increase of loading rate [37]. Therefore, the engineering stress–strain curves shown in Fig. 2 and the properties listed in Table 1 cannot represent the exact differences of the post-necking properties due to the differences of coupon geometries and loading rates in tensile coupon tests. Nevertheless, this paper focuses only on a practical procedure of calibrating the ductile damage model based on the descending stage of engineering stress–strain curves instead of the exact behaviour comparison for each steel. The engineering stress–strain curves shown in Fig. 2 are the resources of the material properties in the following analysis.

2.2. Post-necking stress–strain laws

The pre-necking true stress–strain relation can be converted from the experimental engineering stress–strain curve based on assumptions that the volume of the gauge part remains unchanged and the deformation in the gauge part is uniformly distributed under the pre-necking tensile loading. Eq. (1) is the conversion expressions from engineering stress–strain σ_e-ε_e to true stress–strain σ_t-ε_t. The pre-necking engineering stress–strain relations shown in Fig. 2 are used to derive the pre-necking true stress–strain relations for each steel based on Eq. (1) and numerical pre-necking true stress–strain relations are adopted in the FEA of this study.

$$\sigma_t = \sigma_e(1 + \varepsilon_e) \tag{1.1}$$

$$\varepsilon_t = \ln(1 + \varepsilon_e) \tag{1.2}$$

The post-necking true stress–strain relations cannot be directly inferred from the descending engineering stress–strain curves as the deformations in the necking region would no longer be uniformly distributed due to the strain localization effect. Therefore, using a proper expression to describe and calibrate the post-necking stress–strain relations is of significance. Bridgman [38] proposed an approximation for the post-necking stress–strain relation using actual geometries (diameter and radius of curvature) in the necking region. It is not easy to determine the post-necking stress–strain relation using this method since measuring the radius of curvature in the necking region is rather difficult. In the recent research on calibrating the ductile fracture model of structural steels [15,16], cylindrical coupon tests were conducted and the post-necking true stress–strain relation was assumed as a linear curve from the true stress–strain at the onset of necking to the fracture stress–strain derived upon the fracture diameter at the critical necking section. Both Bridgman's method [38] and the

method used in [15,16] are only applicable to cylindrical coupons rather than commonly-used coupons with a rectangular cross-section.

Ling [39] proposed a combined linear and power stress–strain law to describe the post-necking stress–strain relations, as shown in Eq. (2).

$$\sigma_t = (W)(a\varepsilon_t + b) + (1 - W)(K\varepsilon_t^n) \tag{2}$$

In Eq. (2), $(a\varepsilon_t + b)$ is the linear stress–strain law; $(K\varepsilon_t^n)$ is the power stress–strain law using Hollomon's power expression [40]; W is a weighting factor.

For the linear and power laws in Eq. (2), the stress continuity condition of Eq. (3.1) and the initial necking condition of Eq. (3.2) need to be satisfied simultaneously.

$$\sigma_t|_{\varepsilon_t=\varepsilon_{t,u}} = \sigma_{t,u} \tag{3.1}$$

$$\frac{d\sigma_t}{d\varepsilon_t}\bigg|_{\varepsilon_t=\varepsilon_{t,u}} = \sigma_{t,u} \tag{3.2}$$

In Eq. (3), $\sigma_{t,u}$ and $\varepsilon_{t,u}$ denote the true stress and true strain at the onset of necking, respectively. Then, parameters in linear and power laws can be derived; $a = \sigma_{t,u}$, $n = \varepsilon_{t,u}$, $b = a(1 - n)$, and $K = a/n^n$.

The true stress and strain at the onset of necking for each steel are calculated according to Eq. (1) based on the corresponding engineering stress and strain as marked in Fig. 2. Parameters a, b, K, n in the combined stress–strain law of Eq. (2) can then be calculated except for the weighting factor W, which will be calibrated for each steel in the following analysis. Table 2 lists the true stress and strain at the onset of necking and the corresponding values of parameters in the combined stress–strain law of Eq. (2) for each steel.

There is only one unknown parameter, the weighting factor W, in the combined stress–strain law of Eq. (2) and an appropriate weighting factor can be calibrated for each steel. In [39], the power law and the linear law are considered as the lower and upper bounds for the metallic post-necking true stress–strain relation, respectively. Therefore, the range of validity for weighting factor W is defined between 0 and 1. However, it is found that the power stress–strain law would overestimate the post-necking true stress–strain relations of some steels [33,41], indicating that the power law should not be deemed as the lower bound of post-necking stress–strain relations. Given that the post-necking stress of S690Q would be overestimated using the power stress–strain law in Eq. (2), Ho et al. [33] proposed a piecewise expression for describing the full-range true stress–strain relation of S690Q. The true stress–strain relation was derived using an instantaneous area method through successive corrections of stress–strain according to measured and predicted deformations of tensile coupons, which made it inconvenient for practical use. Jia and Kuwamura [41] proposed a modified weighted average method to describe post-necking stress–strain relations, in which the upper bond of post-necking stress was still described using the linear law in Eq. (2) and the lower bond was taken as a constant equal to the true stress at the onset of necking instead of the power law in Eq. (2).

Table 2
Parameters for post-necking stress–strain curves.

Steel	$\sigma_{t,u}$	$\varepsilon_{t,u}$	a	b	K	n
S355	666.1	0.166	666.1	555.8	897.1	0.166
S690Q	832.9	0.059	832.9	783.6	984.6	0.059
S700MC	919.8	0.091	919.8	836.3	1143.6	0.091
S960Q	1104.6	0.051	1104.6	1048.6	1284.9	0.051

In this paper, the combined linear and power law of Eq. (2) is still adopted to calibrate the post-necking damaged stress–strain relations of each investigated steel, which means that the damage induced by the void growth after necking is considered in the post-necking true stress–strain relations. It is found that the weighting factor W in Eq. (2) could also be less than zero, with which the post-necking true stress–strain relations of each steel could be calibrated. Fig. 3 shows the comparison between engineering and true stress–strain curves of S355. The pre-necking true stress–strain curve is obtained based on Eq. (1), while the post-necking true stress–strain curves are based on Eq. (2) with various assumed weighting factors from −0.5 up to 1.5. The combined linear and power law of Eq. (2) generates a smooth stress–strain transition from pre-necking to post-necking owing to the satisfaction of Eq. (3). With the increase of the weighting factor W, the post-necking stress has an increasing trend at the same strain. Therefore, the only unknown parameter in Eq. (2), weighting factor W, could be calibrated for each steel with values even less than zero or larger than 1.

2.3. Post-necking stress–strain calibrations

Tensile coupon tests on the investigated steels are modelled using ABAQUS package [42], as shown in Fig. 1. The grip parts in both ends are only about 1/3 of the actual dimensions to improve the computing efficiency as stated above. The left and right ends in the modelling are coupled to a reference point at the respective centre by all freedoms. The left reference point is fully fixed, whereas for the right reference point, an axial displacement is applied in the X-direction to realize the tensile loading and other freedoms are fully constrained. Quasi-static analyses on the tensile coupon tests are carried out using the explicit dynamic solver in ABAQUS. Eight node hexahedral solid elements with reduced integration (C3D8R) are used to simulate the behaviour of the tensile coupons. Duration of the tensile loading step is set to 200 s and target time increment is 0.001 s in all calculations. The FEA engineering stress–strain curves are obtained by analysing the elongations

of the gauge length and the force in tension at each time step in the postprocessing.

Material plasticity is input in the simulations in the form of true stress and true plastic strain. The pre-necking and post-necking stress–strain relations are based on Eq. (1) and Eq. (2), respectively. The von Mises criterion is used to describe the yield surfaces with associated plastic flow in the FEA. Different post-necking true stress–strain relations, described by the combined law of Eq. (2) with different weighting factors as shown in Fig. 3 for S355, can generate distinct post-necking FEA engineering stress-stress curves. Therefore, the most appropriate weighting factor in the combined linear and power law of Eq. (2) can be calibrated through comparing the FEA and experimental engineering stress–strain curves for each steel.

Mesh size in gauge parts may also affects the strain localization effect, resulting in some variations in the descending stage of the FEA engineering stress–strain curves. The FEA models with two mesh sizes in the gauge parts are calculated for each steel to investigate the mesh size effects. The investigated steels have three types of coupon geometries as shown in Fig. 1. S690Q coupon has the smallest cross-section in the gauge part, two mesh sizes for S690Q coupon are 0.5 and 0.2 mm, while two mesh sizes for S355, S700MC, and S960Q coupons are 1.0 and 0.5 mm. In the FEA models of HSS coupons with the larger mesh size, there are 240 elements in the cross-section of gauge parts.

Figs. 4–7 show the comparisons between the FEA and experimental engineering stress–strain curves of S355, S690Q, S700MC, and S960Q. The FEA engineering stress–strain curves using three weighting factors with an interval of 0.1 are exhibited, and the engineering stress–strain curve with the intermediate weighting factor is the closest curve to the corresponding experimental curve for each steel. Using a larger weighting factor in the combined law of Eq. (2) results in a higher engineering stress in the descending stage, since a larger weighting factor generates a higher true stress based on Eq. (2). Mesh sizes in the gauge parts have little influence on the descending stages of the experimental engineering stress–strain curves. When the engineering strain is much larger than the fracture strain of each steel, the finer mesh in the simulations would produce a smaller engineering stress compared to the coarser mesh. This indicates that the strain localization effect of the investigated steels is not sensitive to the mesh size in the simulations. The most appropriate weighting factor for describing S355 post-necking stress–strain relation is 0.1, whereas the most appropriate weighting factors for HSS are all less than zero with values equal to −0.3, −0.1, and −0.2 for S690Q, S700MC and S960Q, respectively.

Fig. 8 shows the calibrated true stress-plastic strain curves for each steel. The post-necking stress–strain relations are based on the combined linear and power law of Eq. (2) with the most appropriate weighting factors as shown in Fig. 8. A short phase of stress growth for S960Q and S690Q can be seen after the onset of necking, and then the true stresses gradually decrease with almost the same rate. The true stresses for S700MC and S355 after the onset of necking have a progressively increasing trend. The stress increasing rate after necking for S355 is slightly larger than that for S700MC since a smaller weighting factor is calibrated for the post-necking stress–strain relation of S700MC. The dash line in
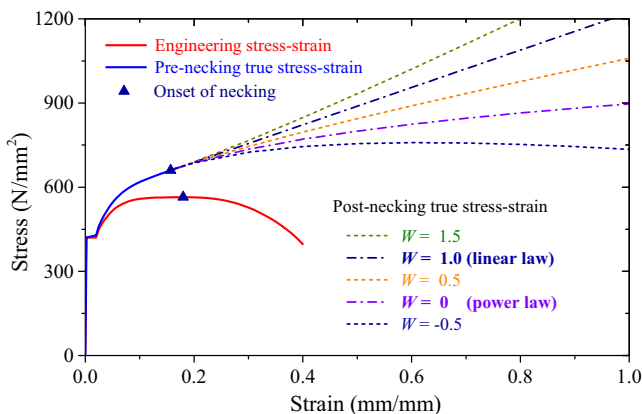
Fig. 3. Comparisons between engineering and true stress–strain of S355.
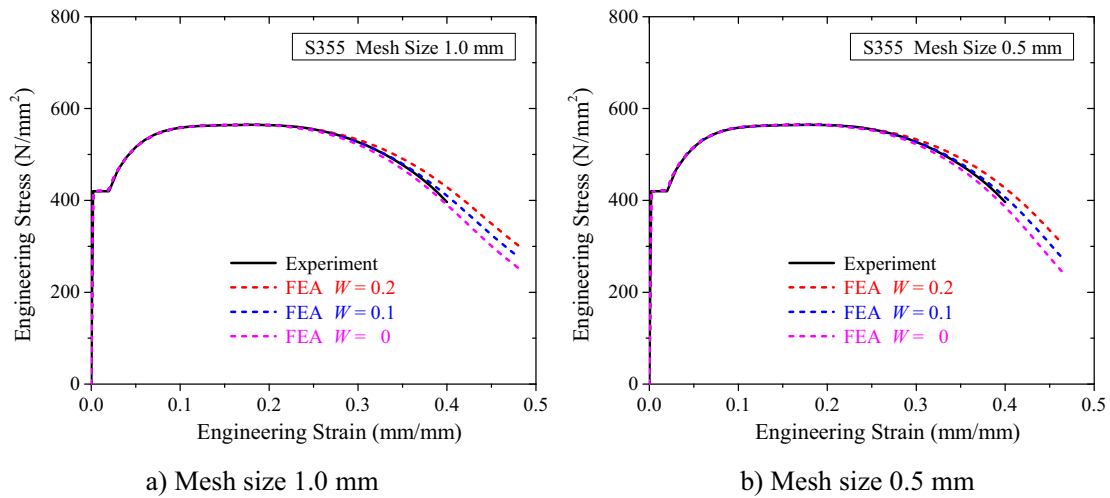
a) Mesh size 1.0 mm   b) Mesh size 0.5 mm

Fig. 4. Weighting factor calibration for S355.

a) Mesh size 0.5 mm   b) Mesh size 0.2 mm
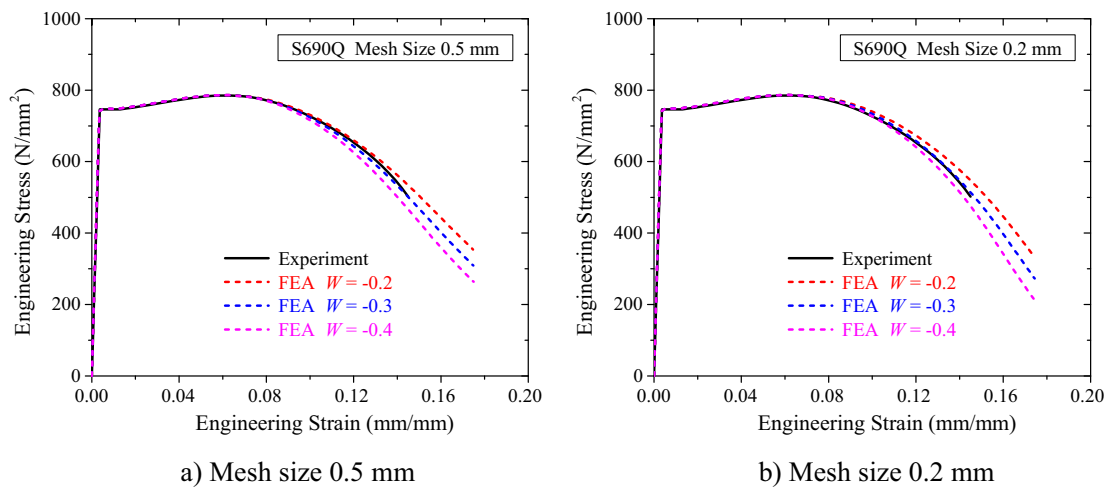
Fig. 5. Weighting factor calibration for S690Q.

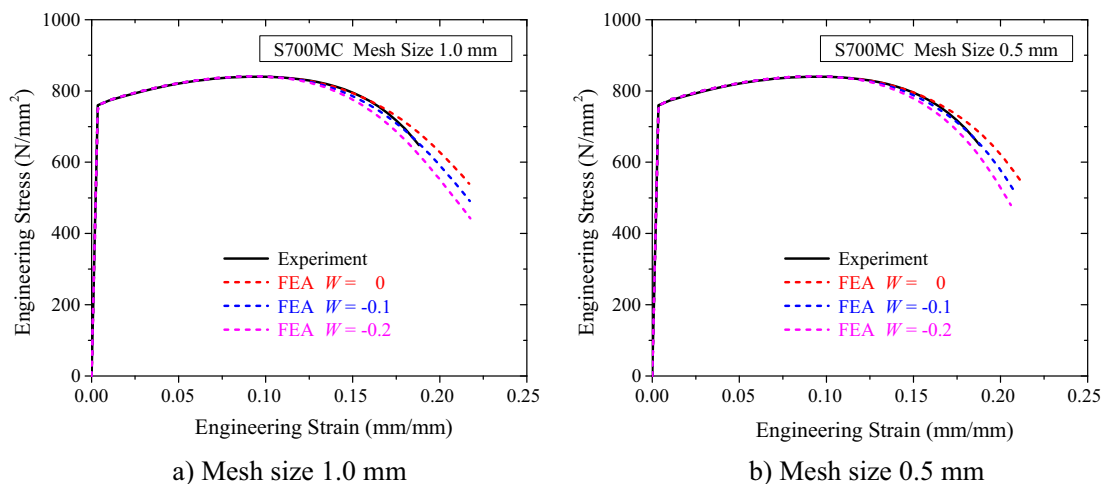a) Mesh size 1.0 mm   b) Mesh size 0.5 mm

Fig. 6. Weighting factor calibration for S700MC steel.

Fig. 8 shows the full-range true stress–strain relation of S690Q which is proposed in [33] with a piecewise expression. It can be seen that the post-necking true stress calibrated based on Eq. (2) is close to the proposed true stress in [33] and the former has a slightly smaller value when the true plastic strain exceeds 0.4. Note that the proposed post-necking true stress–strain curves
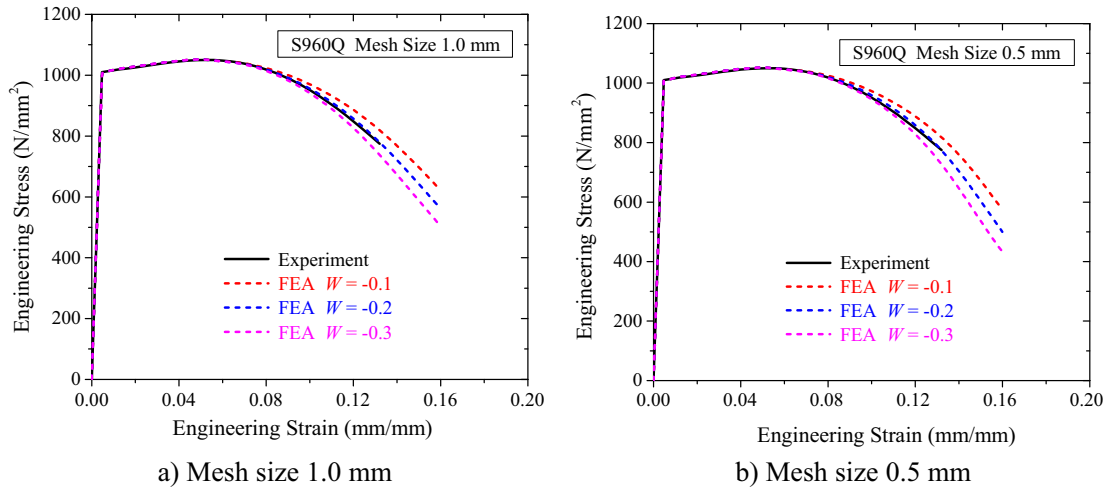
a) Mesh size 1.0 mm

b) Mesh size 0.5 mm

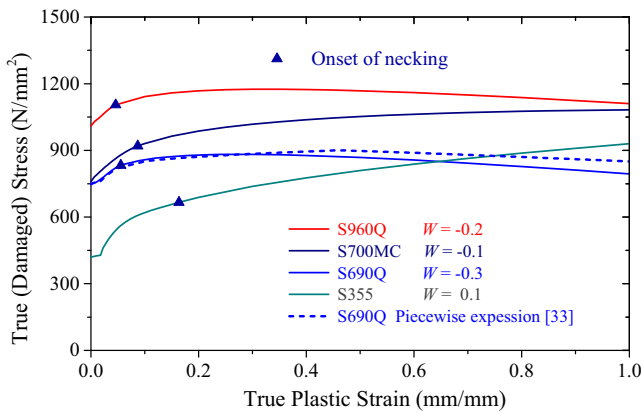**Fig. 7.** Weighting factor calibration for S960Q.

Fig. 8. True stress–strain curves of structural steels.

shown in Fig. 8 have considered the effects of void nucleation and growth during the necking stage, therefore these calibrated stress–strain relations are applicable to the stress modified critical strain (SMCS) model and void growth model (VGM), where the damage induced by void nucleation and growth is incorporated in material constitutive and the fracture initiation due to void coalescence is related to plastic strains and triaxial stresses [12–16].

Fig. 9 shows the deformations and contour plots of equivalent plastic strains (PEEQ) in the necking regions of tensile coupons at respective fracture load, based on the calibrated material plasticity for each steel. The deformations at the necking regions under two mesh sizes are nearly identical for all coupons at respective fracture load. However, the finer mesh in the simulations would lead to a slightly larger PEEQ at the necking regions. For S355 and S690Q coupons with the finer mesh, the maximum PEEQ at the necking regions is about 1.05 times as large as that with the coarser mesh, whereas this ratio is about 1.1 for S700MC and S960Q coupons. The difference may be caused by the different geometries of tensile coupons. Besides, the maximum PEEQ at the necking regions at fracture load is about 0.90 for HSS coupons with the coarser mesh, while S355 coupon with the coarser mesh has a slightly larger value equal to 1.07.

3. Ductile damage models

In the ductile fracture model, such as stress modified critical strain (SMCS) model and void growth model (VGM), it is assumed

that void growth is the major step inducing fracture initiation and void nucleation strains are generally neglected [12–16]. Therefore, using the ductile fracture models only the initial fracture can be predicted. The damage initiation and evolution due to void nucleation and growth cannot be identified accurately since the damage properties are incorporated in the material constitutive as stated above. In this paper, a practical damage model for structural HSS will be calibrated, which is composed of damage initiation criterion and damage evolution law for predicting void nucleation and growth respectively, and a critical damage variable D_{cr} is adopted to predict the initial fracture due to void coalescence. ABAQUS [42] offers a general capability for modelling the progressive damage and failure of steel materials, requiring the specification of (1) the undamaged elastoplastic response, (2) a damage initiation criterion, and (3) a damage evolution law including a choice of element removal. The damage initiation criterion will be introduced firstly as follows.

3.1. Damage initiation criteria

The damage initiation criterion in this paper is to predict the initial damage induced by void nucleation. Note that the "damage initiation criterion" in ABAQUS could also be taken as the fracture initiation criterion in the VGM, which is determined by plastic strains and hydrostatic stresses. It is clear that damage induced by void nucleation will occur when the plastic strain reaches a threshold [29–31], but no expression can be used to predict the damage initiation due to the inconvenience of identifying the plastic strain corresponding to void nucleation. Therefore, it is assumed here that the damage initiation is similarly governed by plastic strains and hydrostatic stresses as the fracture initiation in the VGM, as shown in Eq. (4).

$$\bar{\varepsilon}_D^{pl} = \bar{\varepsilon}_D^{pl}\left(\eta, \dot{\bar{\varepsilon}}^{pl}\right) = \alpha \cdot \exp(-\beta \cdot \eta) \tag{4}$$

In Eq. (4), the equivalent plastic strain (PEEQ) at damage initiation $\bar{\varepsilon}_D^{pl}$ is a function of stress triaxiality η and strain rate $\dot{\bar{\varepsilon}}^{pl}$ as defined in ABAQUS [42]. Stress triaxiality $\eta = -p/q$, p is the pressure stress, q is the Mises equivalent stress. $\dot{\bar{\varepsilon}}^{pl}$ is the rate of PEEQ and its effect on the damage initiation is neglected in this study. The relationship between damage initiation PEEQ $\bar{\varepsilon}_D^{pl}$ and stress triaxiality η is defined as an exponential function according to the
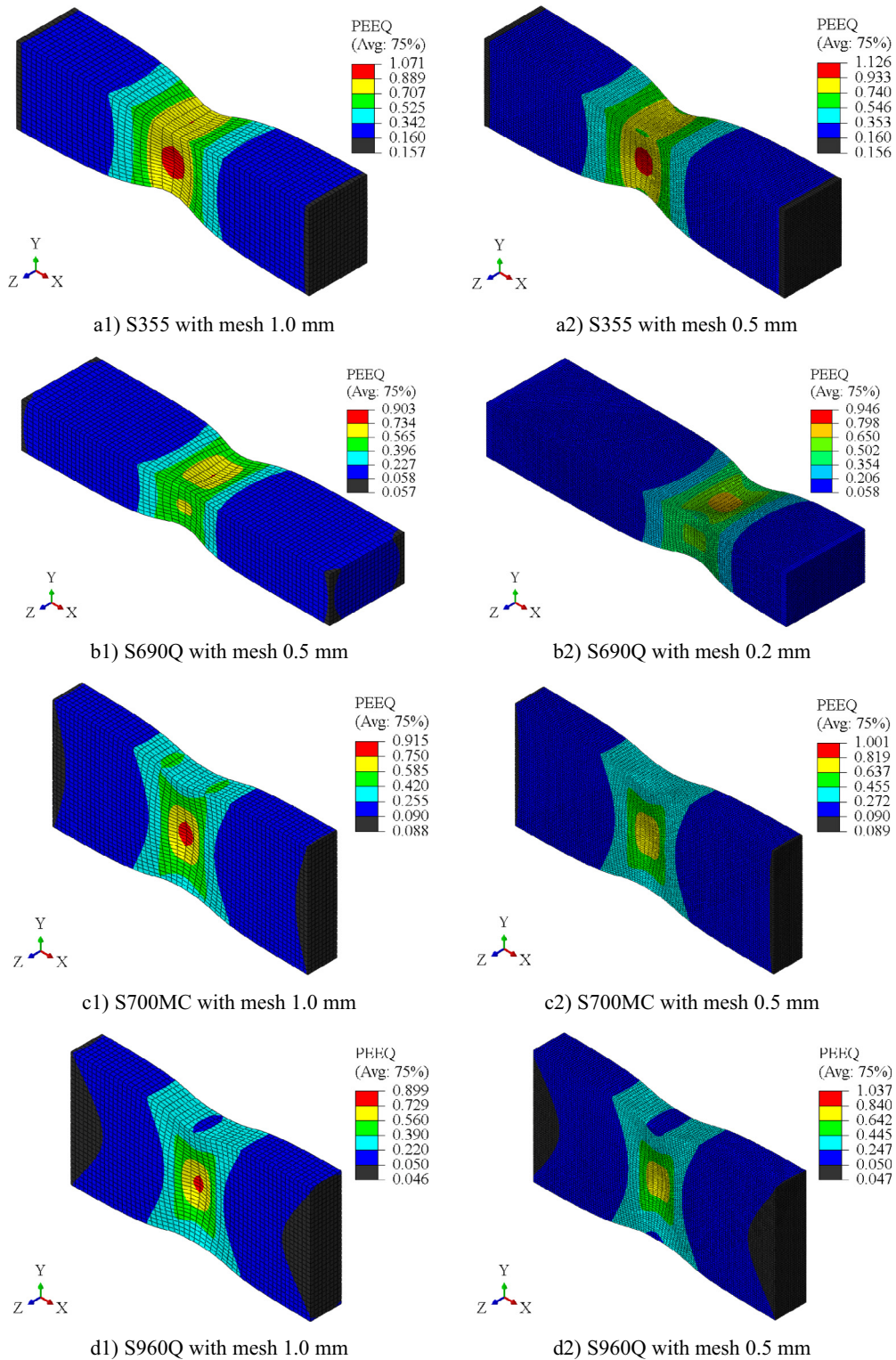
Fig. 9. Deformations and contour plots of equivalent plastic strains at fracture loads.

Rice-Tracey model [43]. α and β are two material parameters. β is generally taken as 1.5 [43,12–16] while the only unknown parameter α could be estimated based on tensile coupon test results. The damage initiation criterion is met when the condition of Eq. (5) is satisfied [42], in which $\bar{\varepsilon}^{pl}$ is the equivalent plastic strain (PEEQ) and ω_D is the damage initiation variable.

$$\omega_D = \int \frac{d\bar{\varepsilon}^{pl}}{\bar{\varepsilon}_D^{pl}\left(\eta, \ \overline{\dot{\varepsilon}^{pl}}\right)} = 1 \tag{5}$$

In tensile coupon tests, the damage initiation due to void nucleation would occur at the onset of necking, which has been observed by Achouri et al. [19]. The stress triaxiality η in the gauge
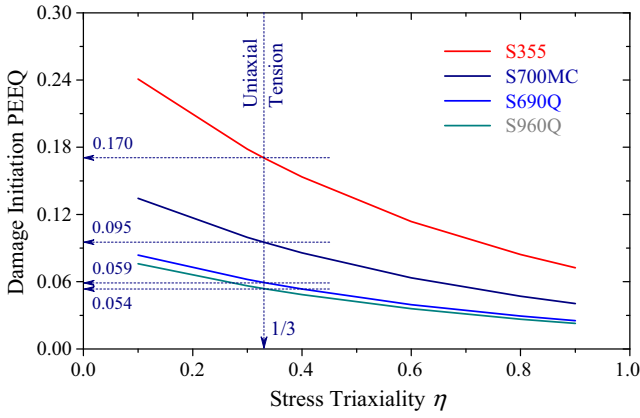
Fig. 10. Damage initiation PEEQ vs. stress triaxiality curves.

part is equal to 1/3 before the occurrence of necking. Accordingly, the damage initiation PEEQ at $\eta = 1/3$ can be taken as the PEEQ $\bar{\varepsilon}_n^{pl}$ of core elements in the coupon necking region at the onset of necking. Then, parameter α can be obtained by Eq. (6). The relationship between damage initiation PEEQ $\bar{\varepsilon}_D^{pl}$ and stress triaxiality η can be expressed by Eq. (7) [44]. Fig. 10 shows the damage initiation PEEQ $\bar{\varepsilon}_D^{pl}$ vs. stress triaxiality η curves for the investigated steels according to Eq. (7). With the increase of stress triaxiality, the damage initiation PEEQ has a gradually decreasing trend. At the same stress triaxiality, S355 has the largest damage initiation PEEQ, followed by S700MC, S690Q, and S960Q.

$$\bar{\varepsilon}_n^{pl} = \alpha \cdot \exp(-1.5 \cdot 1/3) \;\Rightarrow\; \alpha = \frac{\bar{\varepsilon}_n^{pl}}{\exp(-1.5 \cdot 1/3)} \quad (6)$$

$$\bar{\varepsilon}_D^{pl} = \alpha \cdot \exp(-1.5 \cdot \eta) = \bar{\varepsilon}_n^{pl} \cdot \exp[-1.5 \cdot (\eta - 1/3)] \quad (7)$$

3.2. Estimation of undamaged stresses

The true stress–strain curves shown in Fig. 8 have incorporated the damage properties induced by void nucleation and growth, these curves therefore can be taken as the damaged true stress–strain relations for each steel. However, the undamaged stress–strain relations, describing the stress–strain response excluding the damage effects by void nucleation and growth, are necessary for the ductile damage model and will be approximately estimated based on the calibrated damaged stress–strain relations under some assumptions.

First, the volume of a core element at the critical necking region in the FEA model is assumed to be constant neglecting the slight expansion due to large tensile plastic deformation. The expansion of the core element due to void growth in the necking region is not included. Eq. (8) can be obtained.

$$A_{ele0} \cdot L_{ele0} = A_{ele} \cdot L_{ele} \;\Rightarrow\; \frac{A_{ele0}}{A_{ele}} = \frac{L_{ele}}{L_{ele0}} \quad (8)$$

In Eq. (8), A_{ele0}, L_{ele0} are the original area and length of the core element; A_{ele}, L_{ele} are the deformed area and length. The axial strain of the core element ε_{elet} can be estimated as shown in Eq. (9). The elongation of the core element can then be obtained.

$$\varepsilon_{elet} = \int_{L_{ele0}}^{L_{ele}} \frac{dL_{ele}}{L_{ele}} = \ln L_{ele} - \ln L_{ele0} = \ln\left(\frac{L_{ele}}{L_{ele0}}\right) \;\Rightarrow\; \frac{L_{ele}}{L_{ele0}} = \exp(\varepsilon_{elet})$$

A significant assumption introduced in this study is that the same original area in the critical necking region will resist the same axial force in tension in the entire course of tensile loadings. As the same element size is used in the gauge parts of the FEA models, Eq. (10) can be obtained.
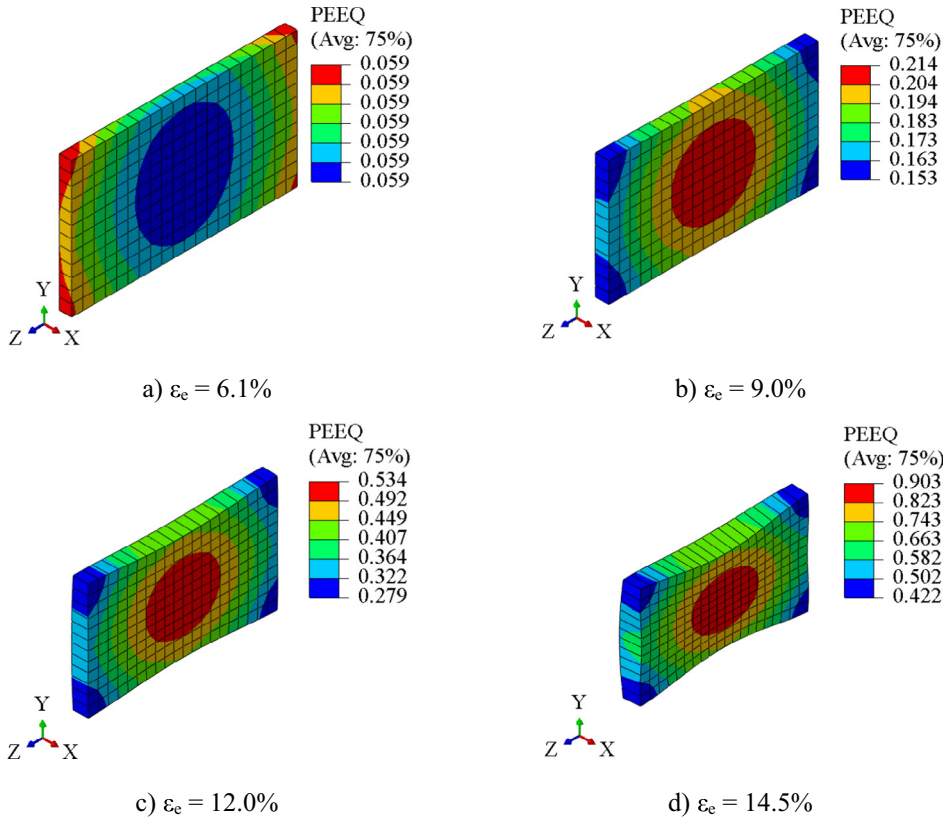

a) $\varepsilon_e = 6.1\%$

b) $\varepsilon_e = 9.0\%$

c) $\varepsilon_e = 12.0\%$

d) $\varepsilon_e = 14.5\%$

Fig. 11. Axial plastic strain of the critical necking elements for S690Q.
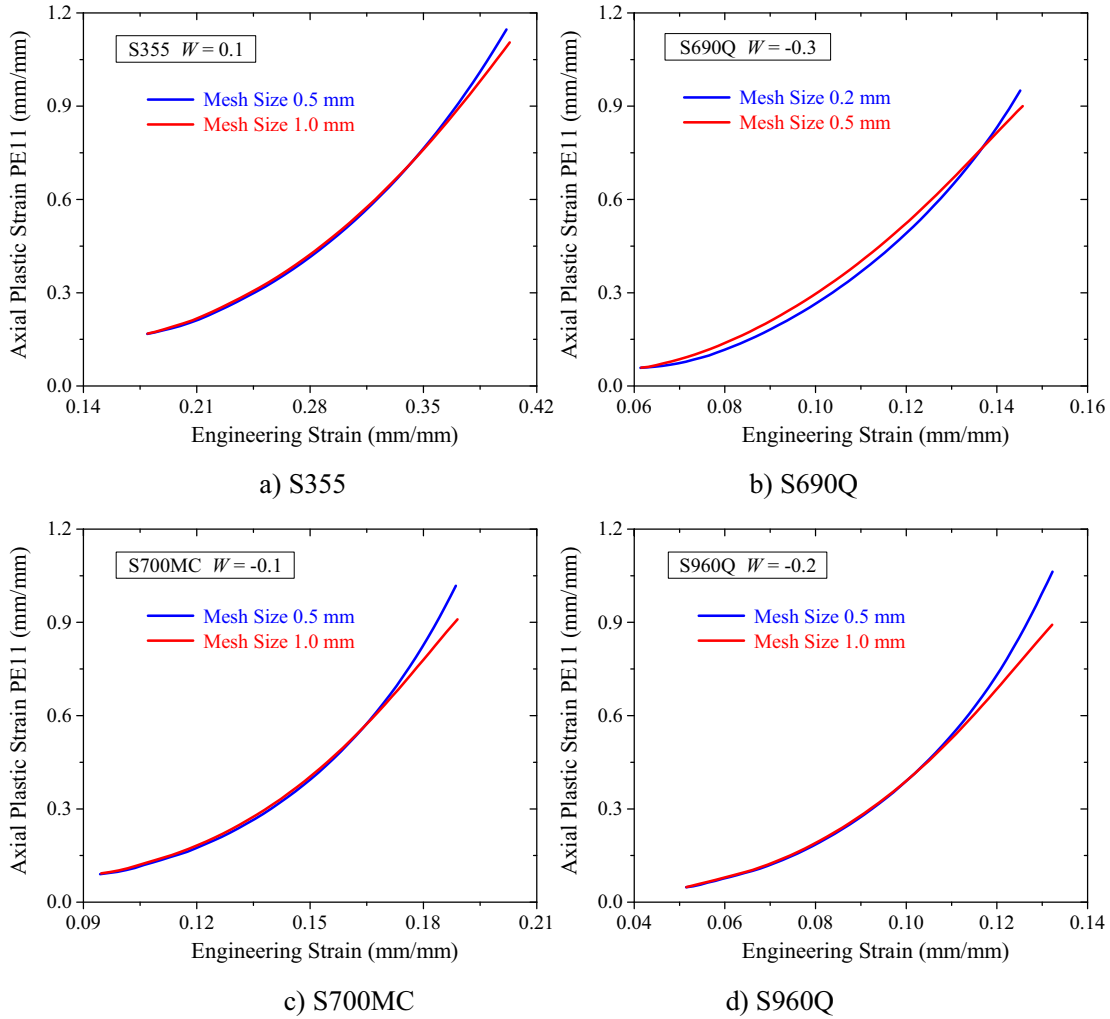
Fig. 12. Relationships between axial maximum plastic strain and engineering strain.

$$\frac{F_{ele}}{A_{ele0}} = \frac{F}{A_0} = \sigma_e \qquad (10)$$

In Eq. (10), F_{ele} denotes the axial tension resisted by a core element, A_{ele0} represents its original area. F denotes the axial tension resisted by the critical necking cross-section, A_0 represents the original area of the cross-section. Then, the undamaged stress σ_{elet} of the core element can be estimated by Eq. (11).

$$\sigma_{elet} = \frac{F_{ele}}{A_{ele}} = \frac{F_{ele}}{A_{ele0}} \cdot \frac{A_{ele0}}{A_{ele}} = \frac{F}{A_0} \cdot \frac{L_{ele}}{L_{ele0}} = \sigma_e \cdot \exp(\varepsilon_{elet}) \qquad (11)$$

Consequently, the undamaged stress σ_{elet} of the core element can be estimated according to the engineering stress σ_e of the tensile coupon and the axial strain ε_{elet} of the core element corresponding to the same engineering strain.

Fig. 11 shows the deformation and equivalent plastic strain (PEEQ) distributions of the elements at the critical necking region for S690Q coupon, corresponding to engineering strains from the initial necking 6.1% to the final fracture 14.5%. The elements in Fig. 11 are those at the critical necking region in Fig. 9c with mesh size 0.5 mm. It can be seen that the PEEQ distribution at the critical necking region is almost uniform at the onset of necking and the distribution would be increasingly uneven as the increase of the engineering strain. The PEEQ of the core elements in the critical necking region is larger than that of the peripheral elements from the onset of necking to the final fracture. This indicates that the

final fracture will take place initially from the core of the necking region. From the simulation of S690Q coupon with mesh size 0.5 mm, the relationship between the axial strain of the core elements and the corresponding engineering strain can be obtained.

From the tensile coupon simulations using the calibrated post-necking stress–strain relations, the relationships between the axial plastic strain (PE11) of the core elements at the critical necking region and the corresponding engineering strain can be extracted for each steel, see Fig. 12. As the increase of the engineering strain, the PE11 of the core elements at the critical necking region gets larger with an increasing growth rate for each steel. When the engineering strain approaches the fracture engineering strain, the PE11 of the core elements in the calculation with finer mesh will be larger than that in the calculation with coarser mesh for each steel. This indicates that the strain distributions in the necking region are sensitive to the mesh size when the engineering strains are close to the fracture engineering strains. The effects of the mesh size can be neglected when the engineering strains are much less than the fracture engineering strains.

The undamaged stress of the core elements at the critical necking region can be estimated using Eq. (11) and the curves shown in Fig. 12. Fig. 13 shows the estimated undamaged stress vs. the PEEQ of the core elements at the critical necking region. The finer mesh in the calculations generates slightly larger undamaged stress when the coupons approach the final fracture. In most cases, the effects of mesh size can be neglected. Besides, it is found that the
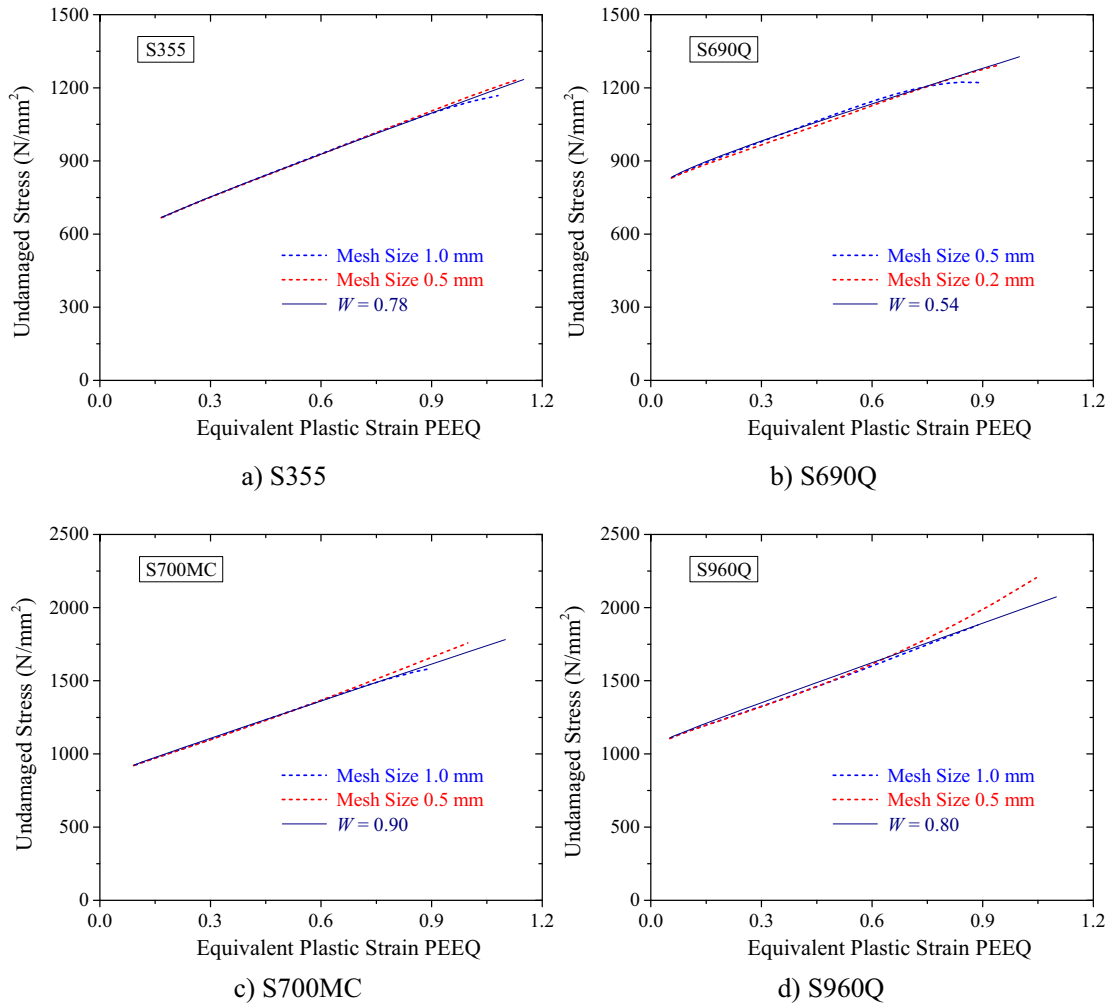
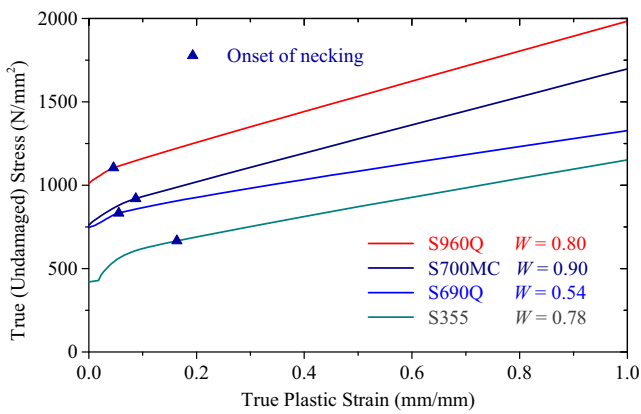**Fig. 13.** Relationships between predicted undamaged stress and PEEQ.

Fig. 14. Estimated undamaged true stress of each steel.
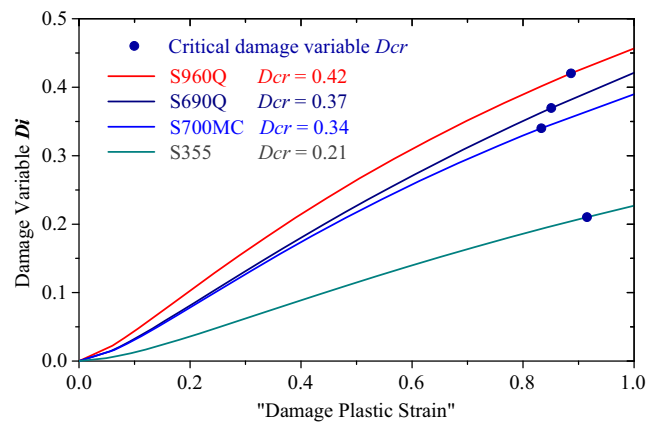

Fig. 15. Relationships between damage variable and "damage plastic strain".

estimated undamaged stress for each steel could also be described using the combined linear and power law of Eq. (2) with calibrated weighting factors. As shown in Fig. 13, the weighting factors in the combined law of Eq. (2) for describing the undamaged stress of S355, S690Q, S700MC, and S960Q are 0.78, 0.54, 0.90, and 0.80, respectively. Fig. 14 shows the estimated undamaged stress–strain curves for the investigated steels. The undamaged stresses for S960Q, S700MC, and S355 have a nearly linearly increasing trend after the onset of necking due to the weighting factors close to 1.0.

3.3. Damage evolution laws

In the above analyses, the calibrated damaged stress and the estimated undamaged stress for the investigated steels after necking have been obtained and expressed by the combined linear and power stress–strain law with corresponding weighting factors. The damage evolution law is related to the damaged and undamaged stress in ABAQUS, which describes the degradation rate of material
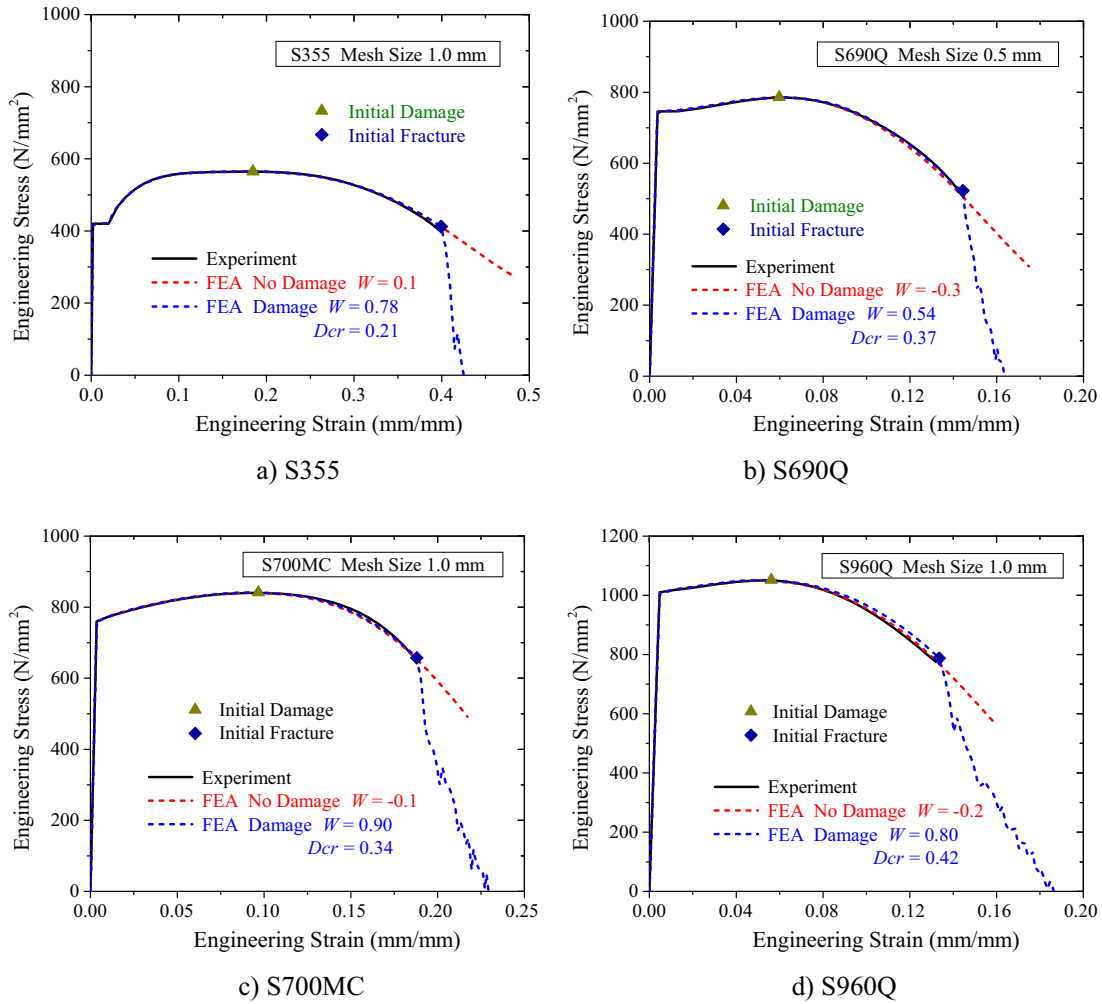
Fig. 16. Engineering stress–strain comparisons between experimental and FEA results.

stiffness once the damage initiation criterion is reached. The degradation of material stiffness is modelled using a scalar damage variable D_i [42]. At any given analysing time, the stress in the material is given by the scalar damage equation as shown in Eq. (12).

$$\sigma_i = (1 - D_i)\bar{\sigma}_i \tag{12}$$

In Eq. (12), $\bar{\sigma}_i$ is the undamaged true stress, which has been estimated and described by the combined stress–strain law shown in Fig. 14; σ_i is the damaged true stress shown in Fig. 8. As the damaged true stress σ_i and the estimated undamaged stress $\bar{\sigma}_i$ have been obtained in the above analyses, the damage variable D_i for each steel can be calculated by Eq. (13).

$$D_i = 1 - \frac{\sigma_i}{\bar{\sigma}_i} \tag{13}$$

Damage evolution law is input in ABAQUS in tabular form as damage variable D_i in function of the effective plastic displacement $\bar{u}_i^{pl}$. The value of $\bar{u}_i^{pl}$ corresponding to D_i is defined by Eq. (14) [42].

$$\bar{u}_i^{pl} = L_{char} \cdot \left(\bar{\varepsilon}_i^{pl} - \bar{\varepsilon}_D^{pl} \right) \tag{14}$$

In Eq. (14), L_{char} is the element characteristic length. For C3D8R element with cubic geometry in the simulations, its characteristic length L_{char} is assumed equal to element edge length same as the mesh size. $\bar{\varepsilon}_i^{pl}$ is the PEEQ, $\bar{\varepsilon}_D^{pl}$ is the damage initiation PEEQ, and $(\bar{\varepsilon}_i^{pl} - \bar{\varepsilon}_D^{pl})$ is the "damage plastic strain".

Fig. 15 shows the damage evolution laws for the investigated steels, which are the relationships between the damage variable D_i and the "damage plastic strain" $(\bar{\varepsilon}_i^{pl} - \bar{\varepsilon}_D^{pl})$ for each steel. The damage evolution laws are obtained from the FEA results with the coarse mesh size. It can be observed that the damage variable D_i has an approximately linear-increasing trend as the increase of the "damage plastic strain" for each steel. At the same "damage plastic strain", the damage variable D_i for S960Q has the maximum values followed by S690Q and S700MC. S355 has minimum damage variables. The critical damage variable D_{cr} is utilized here to realize the "element removal" function in ABAQUS. Its value can be calculated based on Eq. (13) using the damaged and undamaged stresses corresponding to the fracture engineering strain. As elements reach this level of degradation, with damage variable D_i close to the critical damage D_{cr}, the elements will be deleted from the FEA models to simulate the fracture of tensile coupons. The critical damage variables D_{cr} for S960Q, S690Q, S700MC, and S355 are 0.42, 0.37, 0.34, and 0.21, respectively, as marked in Fig. 15. The investigated HSS have much larger critical damage variables compared to mild steel S355. The critical damage variable of S700MC is a little smaller than that of S690Q.
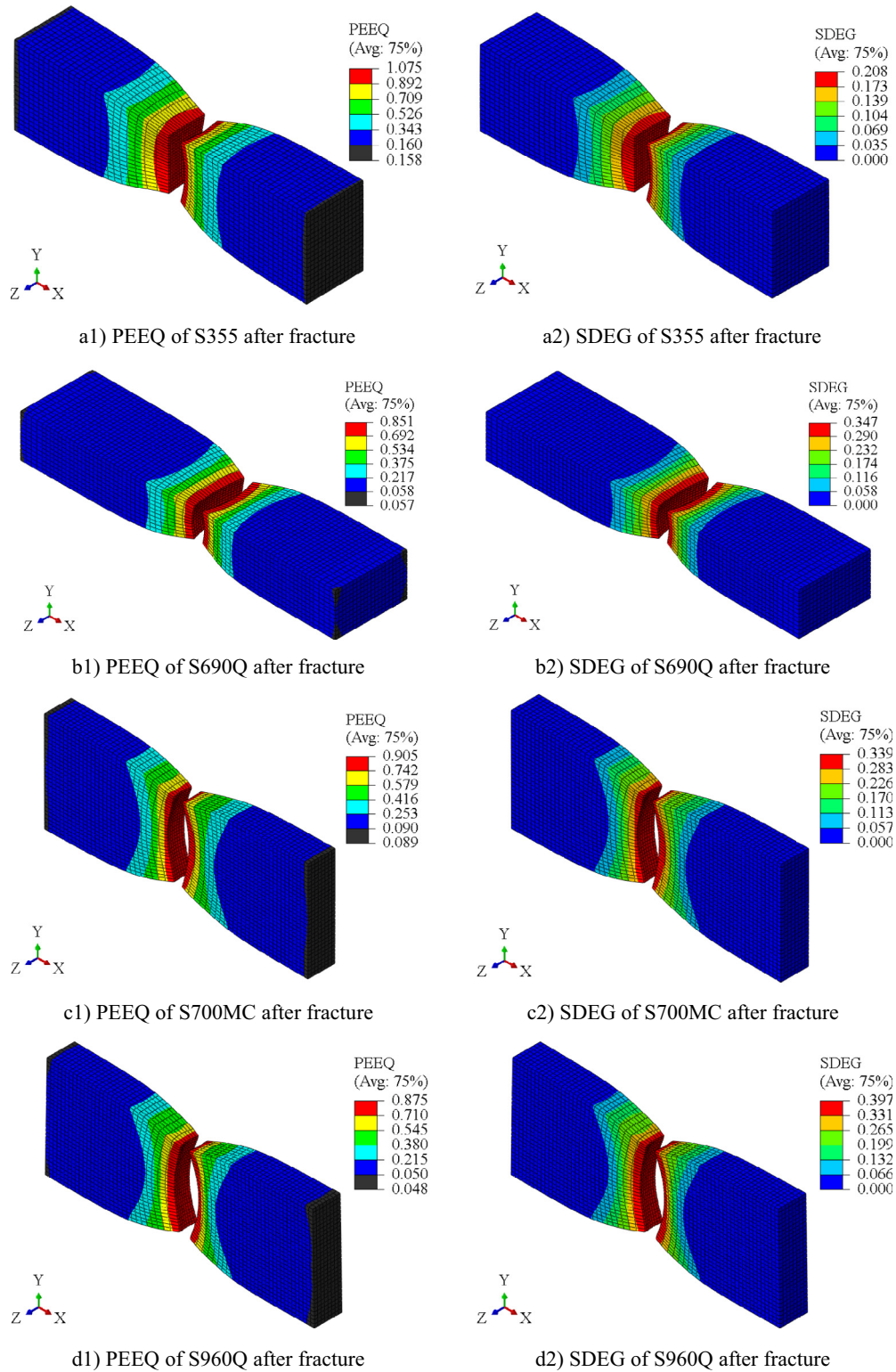
a1) PEEQ of S355 after fracture

a2) SDEG of S355 after fracture

b1) PEEQ of S690Q after fracture

b2) SDEG of S690Q after fracture

c1) PEEQ of S700MC after fracture

c2) SDEG of S700MC after fracture

d1) PEEQ of S960Q after fracture

d2) SDEG of S960Q after fracture

Fig. 17. Contour plots of PEEQ and damage variable for each steel after fracture.

4. FEA results

4.1. Engineering stress–strain curves

The tensile coupon tests on the structural steels are modelled incorporating the proposed ductile damage models. The undam-aged stress–strain curves, shown in Fig. 14, are input as the material plasticity. The damage initiation criteria shown in Fig. 10 and the damage evolution laws shown in Fig. 15 are input as the ductile damage models. Besides, the critical damage variables D_{cr} shown in Fig. 15 are incorporated in the simulations to realize the fracture of tensile coupons. The same quasi-static analyses are conducted

using the explicit dynamic solver in ABAQUS. The FEA engineering stress–strain curves of the structural steels using the proposed ductile damage models could then be obtained.

Fig. 16 shows the comparisons of engineering stress–strain curves between the experimental and FEA results with and without the proposed ductile damage models. Both the FEA results generate very good predictions for the load-descending phases of the tensile coupon test results. The difference of the FEA results with and without the ductile damage models is that using the ductile damage model can simulate the sudden fracture of tensile coupons by defining the critical damage variable D_{cr} for each structural steel.

4.2. Fracture modes

In the FEA results incorporating the proposed ductile damage models, the damage variable of the elements in the necking region would gradually grow up to the critical damage variable as the increase of the axial displacement. When the damage variable of the elements in the critical necking region reaches the defined critical damage variable, the elements will be deleted from the FEA model to simulate the sudden fracture of tensile coupons. Fig. 17 exhibits the final fracture modes of tensile coupons using the proposed ductile damage models. The figures in the left of Fig. 17 show the PEEQ contour plots in the necking region of tensile coupons after fracture. The right figures show the damage variable (SDEG) contour plots in the necking region of tensile coupons after fracture. The PEEQ distributions in Fig. 17 for each steel can be made a comparison with the PEEQ distributions in the left of Fig. 9. It can be seen that using the proposed ductile damage models could generate almost the same PEEQ distributions in the necking region for each steel compared to the results without damage models. The maximum SDEG in the necking region for each coupon after fracture is slightly less than the respective critical damage variable D_{cr}, because the elements reaching the critical damage variable D_{cr} have been deleted from the mesh of the model, as shown in the right of Fig. 17. The calibrated ductile damage models for structural steels have been used to simulate the behaviours of S700MC and S960Q centre-holed plates under tensile loading [45]. Using the proposed ductile damage models could generate almost the same numerical load–displacement curves as using the Void Growth Model (VGM), which are very close to the experimental curves. The initial fracture, determining the deformation capacity of the centre-holed plates, could be accurately predicted using the proposed ductile damage models.

5. Conclusions

In this paper, the ductile damage models for S355 and HSS S690Q, S700MC, S960Q were established based on the available tensile coupon test results in the literature. A combined linear and power law was used to describe the post-necking damaged and undamaged stress–strain relations for each steel with the calibrated weighting factors. The effects of mesh size on the strain localization were investigated. The ductile damage properties for the investigated steels were made a comparison. The following conclusions are drawn from the analysis of this paper.

1) The combined linear and power law of Eq. (2) can be used to describe the post-necking stress–strain relations of S355 and HSS S690Q, S700MC, S960Q with weighting factors equal to 0.1 and −0.3, −0.1, −0.2, respectively. For S690Q and S960Q, their post-necking true stresses have a short phase of growing followed by a gradually decreasing trend until the final fracture. For S700MC and S355, their post-necking true

stresses have a progressively increasing trend until the final fracture.

2) The post-necking undamaged stress–strain relations are estimated according to the relationship between engineering stress–strain and axial strain of the core elements at critical necking regions of tensile coupons. The estimated post-necking undamaged stress–strain relations could also be described using the combined linear and power law of Eq. (2). The undamaged true stresses for S960Q, S700MC, and S355 have a nearly linear-increasing trend after the onset of necking due to the weighting factors close to 1.0.

3) The ductile damage models are established based on the calibrated damaged stress–strain relations and the estimated undamaged stress–strain relations. It is verified that the full-range engineering stress–strain curves and the fracture modes of the investigated steels can be accurately predicted using the proposed ductile damage models.

4) The damage variable for each steel has an approximately linear-increasing trend as the increase of the "damage plastic strain". The investigated HSS are more susceptible to damage compared to mild steel S355. The damage variable of S960Q is about 2 times as large as that of S355 from the onset of necking to final fracture.

CRediT authorship contribution statement

Fei Yang: Visualization, Methodology, Investigation, Validation, Formal analysis, Writing - original draft. **Milan Veljkovic:** Resources, Supervision, Writing - review & editing. **Yuqing Liu:** Conceptualization, Supervision, Writing - review & editing.

Declaration of Competing Interest

The authors declare that they have no known competing financial interests or personal relationships that could have appeared to influence the work reported in this paper.

Acknowledgements

References

[1] L. Jensen, M.L. Bloomstine, Application of high strength steel in super long span modern suspension bridge design, Proceedings of the Nordic Steel Construction Conference, Malmö, Sweden, 2009, pp. 494–501.

[2] A.T. Tran, M. Veljkovic, C. Rebelo, L.S. da Silva, Resistance of cold-formed high strength steel circular and polygonal sections – Part 1: Experimental investigations, J. Constr. Steel Res. 120 (2016) 245–257.

[3] H.Y. Ban, G. Shi, A review of research on high-strength steel structures, Proc. Inst. Civil Eng. – Struct. Build. 171 (2017) 625–641.

[4] T. Mueller, B. Straetmans, High strength seamless tubes and steel hollow sections for cranes and machine building applications-production and properties, Stahlbau 84 (2015) 650–654.

[5] EN 10025-4, Hot rolled products of structural steels – Part 4: Technical delivery conditions for thermomechanical rolled weldable fine grain structural steels, European Committee for Standardization, Brussels, Belgium, 2004.

[6] EN 10025-6, Hot rolled products of structural steels – Part 6: Technical delivery conditions for flat products of high yield strength structural steels in the quenched and tempered condition, European Committee for Standardization, Brussels, Belgium, 2004.

[7] R. Willms, High strength steel for steel constructions, Proceedings of the Nordic Steel Construction conference, Malmö, Sweden, 2009, pp. 597–604.

[8] P. Može, D. Beg, J. Lopatič, Net cross-section design resistance and local ductility of elements made of high strength steel, J. Constr. Steel Res. 63 (2007) 1431–1441.

[9] P. Može, D. Beg, High strength steel tension splices with one or two bolts, J. Constr. Steel Res. 66 (2010) 1000–1010.

[10] D. Schäfer, B. Eichler, L. Amlung, I. Vayas, V. Karlos, A. Spiliopoulos, M. Lippe, Z. Kubon, L. Kander, Modern plastic design for steel structures, Final report, RFSR-CT-2005-00039, 2008.

[11] M. Gkantou, M. Theofanous, C. Baniotopoulos, Plastic design of hot-finished high strength steel continuous beams, Thin-Walled Struct. 133 (2018) 85–95.

[12] A.M. Kanvinde, G.G. Deierlein, The void growth model and the stress modified critical strain model to predict ductile fracture in structural steels, J. Struct. Eng. 132 (12) (2006) 1907–1918.

[13] A.M. Kanvinde, G.G. Deierlein, Finite-element simulation of ductile fracture in reduced section pull-plates using micromechanics-based fracture models, J. Struct. Eng. 133 (5) (2007) 656–664.

[14] A.T. Myers, A.M. Kanvinde, G.G. Deierlein, Calibration of the SMCS criterion for ductile fracture in steels: specimen size dependence and parameter assessment, J. Eng. Mech. 136 (11) (2010) 1401–1410.

[15] F. Liao, M. Wang, L. Tu, J. Wang, L. Lu, Micromechanical fracture model parameter influencing factor study of structural steels and welding materials, Constr. Build. Mater. 215 (2019) 898–917.

[16] Q. Han, K. Jiang, J. Wen, L. Yang, Micromechanical fracture models of Q345 steel and its weld, J. Mater. Civ. Eng. 31 (11) (2019) 04019268.

[17] A.L. Gurson, Continuum theory of ductile rupture by void nucleation and growth: Part I – Yield criteria and flow rules for porous ductile media, J. Eng. Mater. Technol. 99 (1) (1977) 2–15.

[18] A. Needleman, V. Tvergaard, An analysis of ductile rupture in notched bars, J. Mech. Phys. Solids 32 (6) (1984) 461–490.

[19] M. Achouri, G. Germain, P. Dal Santo, D. Saidane, Experimental characterization and numerical modeling of micromechanical damage under different stress states, Mater. Des. 50 (2013) 207–222.

[20] M. Achouri, G. Germain, P. Dal Santo, D. Saidane, Experimental and numerical analysis of micromechanical damage in the punching process for high-strength low-alloy steels, Mater. Des. 56 (2014) 657–670.

[21] M. Feldmann, S. Schaffrath, Assessing the net section resistance and ductility requirements of EN 1993-1-1 and EN 1993-1-12, Steel Constr. 10 (2017) 354–364.

[22] M. Feldmann, S. Schaffrath, Application of damage theory to structures made from high-strength steels, Steel Constr. 11 (2018) 257–263.

[23] Y. Huang, B. Young, The art of coupon tests, J. Constr. Steel Res. 96 (2014) 159–175.

[24] S. Hertelé, W. De Waele, R. Denys, A generic stress-strain model for metallic materials with two-stage strain hardening behaviour, Int. J. Non Linear Mech. 46 (2011) 519–531.

[25] X. Yun, L. Gardner, Stress-strain curves for hot-rolled steels, J. Constr. Steel Res. 133 (2017) 36–46.

[26] L. Gardner, X. Yun, Description of stress-strain curves for cold-formed steels, Constr. Build. Mater. 189 (2018) 527–538.

[27] M. Paredes, T. Wierzbicki, P. Zelenak, Prediction of crack initiation and propagation in X70 pipeline steels, Eng. Fract. Mech. 168 (2016) 92–111.

[28] C.C. Roth, D. Mohr, Ductile fracture experiments with locally proportional loading histories, Int. J. Plast. 79 (2016) 328–354.

[29] G. Le Roy, J.D. Embury, G. Edwards, M.F. Ashby, A model of ductile fracture based on the nucleation and growth of voids, Acta Metall. 29 (8) (1981) 1509–1522.

[30] J. Lemaitre, A continuous damage mechanics model for ductile fracture, J. Eng. Mater. Technol. 107 (1985) 83–89.

[31] A. Öchsner, Continuum Damage and Fracture Mechanics, Springer, Singapur, 2016.

[32] J. Ribeiro, A. Santiago, C. Rigueiro, Damage model calibration and application for S355 steel, Proc. Struct. Integrity 2 (2016) 656–663.

[33] H.C. Ho, K.F. Chung, X. Liu, M. Xiao, D.A. Nethercot, Modelling tensile tests on high strength S690 steel materials undergoing large deformations, Eng. Struct. 192 (2019) 305–322.

[34] M. Feldmann, N. Schillo, S. Schaffrath, et al., Rules on high strength steel, Final report, RFSR-CT-2012-00036, 2016.

[35] EN 10149-2, Hot rolled flat products made of high yield strength steels for cold forming – Part 2: Technical delivery conditions for thermo-mechanically rolled steels, European Committee for Standardization, Brussels, Belgium, 2013

[36] EN 10025-2, Hot rolled products of structural steels - Part 2: Technical delivery conditions for non-alloy structural steels, European Committee for Standardization, Brussels, Belgium, 2004.

[37] X. Yang, H. Yang, Z. Lai, S. Zhang, Dynamic tensile behaviour of S690 high-strength structural steel at intermediate strain rates, J. Constr. Steel Res. 168 (2020) 105961.

[38] P.W. Bridgman, Studies in Large Plastic Flow and Fracture, McGraw-Hill, New York, 1952.

[39] Y. Ling, Uniaxial true stress-strain after necking, AMP J. Technol. 5 (1996) 37–48.

[40] J.H. Hollomon, Tensile deformation, Trans AIME 162 (1945) 268–290.

[41] L.J. Jia, H. Kuwamura, Ductile fracture simulation of structural steels under monotonic tension, J. Struct. Eng. 140 (5) (2014) 04013115.

[42] Abaqus analysis user's guide, version 6.13. Dassault Systèmes Simulia Corp., Providence, RI, USA, 2013.

[43] J.R. Rice, D.M. Tracey, On the enlargement of voids in triaxial stress fields, J. Mech. Phys. Solids 17 (1969) 201–217.

[44] M. Pavlović, Z. Marković, M. Veljkovic, D. Buđevac, Bolted shear connectors vs. headed studs behaviour in push-out tests, J. Constr. Steel Res. 88 (2013) 134–149.

[45] F. Yang, M. Veljkovic, Y.Q. Liu, Ductile damage modelling of high-strength centre-holed plates under tension, (Under review).